NANO LETTERS

2007
Vol. 7, No. 5
1246−1250

3-D X-ray Diffraction Imaging with Nanoscale Resolution Using Incoherent Radiation

Andrei Y. Nikulin,*,† Ruben A. Dilanian,† Nadia A. Zatsepin,† Brian M. Gable,‡ Barry C. Muddle,‡ Alexei Y. Souvorov,|| Yoshinori Nishino,§ and Tetsuya Ishikawa§

School of Physics, Monash University, Clayton, Victoria 3800, Australia, Department of Materials Engineering, Monash University, Clayton, Victoria 3800, Australia, SPring-8/JASRI, 1-1-1 Kouto, Mikazuki, Sayo-gun, Hyogo 679-5148, Japan, and SPring-8/RIKEN, 1-1-1 Kouto, Mikazuki, Sayo-gun, Hyogo 679-5148, Japan

Received January 17, 2007; Revised Manuscript Received March 19, 2007

ABSTRACT

A novel approach to X-ray diffraction data analysis for nondestructive determination of the shape of nanoscale particles and clusters in three-dimensions is illustrated with representative examples of composite nanostructures. The technique is insensitive to the X-ray coherence, which allows 3-D reconstruction of a modal image without tomographic synthesis and in situ analysis of large (over a several cubic millimeters) volume of material with a spatial resolution of few nanometers, rendering the approach suitable for laboratory facilities.

A feature of emerging nanotechnology has been the development of enhanced capability for the production of a broad and diverse range of materials in the form of nanoscale (<100 nm) particulate, and for the dispersion of such nanoparticulate in a variety of matrices to create novel composite nanostructures. When both particulate dimensions and spacings are nanoscale, there is an enhanced potential for the creation of systems with truly novel structural and/or functional performance, for the scaling laws that govern structure−property relationships in materials of conventional structural scale may no longer apply.[1] Aside from any effects that constrained dimensions may have on the behavior of the constituent phases alone or in combination, the increase in the area of internal interface between the constituents is such that the properties of these interfaces may come to dominate the properties of any hybrid structure. Nanocomposite materials with novel structural, electrical, electronic, optical, and magnetic properties have been recorded, and they are finding applications as diverse as, for example, cosmetics, protective coatings, advanced sensors, new generations of lightweight alloys, and novel biomedical therapeutics and drug delivery systems.

The emergence of this new class of materials brings with it an imperative for improved techniques of structural characterization. The properties of a given composite are a function of the properties of the constituent phases, with the form of the function determined by the form, scale, orientation, and distribution of the dispersed constituent. When the critical structural dimensions are measured in microns (10^{-4}−10^{-6}m), then optical microscopy combined with conventional X-ray diffraction techniques are sufficient to resolve the microstructural features, and determine the structural dimensions and orientation of individual domains. When the features become nanoscale (10^{-7}−10^{-9}m), such characterization typically requires high-resolution electron microscopy, combined with sophisticated electron diffraction techniques. The spatial resolution of a modern field-emission gun (FEG) scanning electron microscope (SEM) is subnanometer, while that of a FEG transmission electron microscope (TEM) is better than 0.1 nm. However, such techniques invariably require specimens that are destructive of a nanocomposite sample and imaging is commonly restricted to projections from 2-D sections. In the TEM, characterization of interface form and structure is limited to small local areas and is highly dependent upon obtaining suitable imaging and diffraction conditions.[2]

Alternative characterization techniques, such as the three-dimensional atom probe (3-DAP), while allowing 3-D atomic reconstruction with sensitivity to chemistry,[3] provide only indirect evidence of particle form and are limited in the volume of material analyzed (~0.01 μm^3) and the nature of samples that can be examined. Others, such as conventional

* Corresponding author. E-mail: Andrei.Nikulin@sci.monash.edu.au.
† School of Physics, Monash University.
‡ Department of Materials Engineering, Monash University.
|| SPring-8/JASRI.
§ SPring-8/RIKEN.

10.1021/nl070131z CCC: $37.00
Published on Web 04/10/2007

small-angle X-ray scattering (SAXS) or grazing incidence SAXS, provide average particle dimensions and, indeed, real-time monitoring of changes in particle dimensions,[4] but do not permit direct observation of particle shapes. There is, at present, no one technique which permits direct, nondestructive 3-D characterization of the form, dimensions, and structure of an embedded dispersion of nanoparticles and their surface topography.

To meet this need for a nondestructive imaging technique of the required resolution, a number of methods using high-energy X-ray[5−22] or electron[23−25] beams are under development for the imaging of non-periodic nanoscale objects and nanostructured materials. One such approach to 3-D microscopy[18−22] employs a refractive zone plate to focus a beam of either soft (0.25−2.0 keV) or hard (3.0−30 keV) X-rays at the sample, with spatial resolutions of <10 nm for soft X-rays and <30 nm for higher energy probes in prospect.[20,22] Such systems may be operated in scanning or full-field transmission modes to permit coherent diffraction and imaging utilizing either absorption or phase contrast and X-ray photon and fluorescence spectroscopies. In an alternative approach, commonly referred to as coherent diffraction imaging (CDI), an iterative oversampling algorithm of modified Gerchberg−Saxton (G−S) type[5] has been shown[6−22] to permit reconstruction of 2-D and 3-D images from the diffraction pattern of a scattering object exposed to a fully coherent X-ray beam. However, both of these experimental approaches to the 3-D X-ray microscopy require a high-energy X-ray source[7−8] with transverse and longitudinal coherence lengths commensurate with the dimensions of the diffracting object.[15] This restricts the systematic characterization of technologically important nanostructures to high-end third generation synchrotrons. However, when the particle size is nanoscale or the particles comprise light elements (as opposed to gold[9] or lead[17]) even the most powerful existing synchrotrons do not produce sufficient brilliance to permit detection of individual particles using CDI.

The novel alternative approach presented here utilizes a wavelength-dispersive crystal analyzer interposed between the object and the detector to effectively deconvolute coherent components of the complex diffraction pattern from an aperiodic array of scattering objects and selectively project the resulting Fraunhofer diffraction pattern in a reciprocal space defined by the position and orientation of the analyzing crystal. It exploits the 3-D geometrical construction of the Ewald sphere to record multiple 2-D distributions of coherent diffracted intensity at different locations on the Ewald sphere (Figure 1). Differences in intensity at known locations in reciprocal space can be analyzed to retrieve phase and synthesize a complete 3-D rendering of the representative of the modal scattering object with nanoscale spatial resolution. The data are recorded in spherical coordinates of reciprocal space using an analyzer−detector arrangement with a large (up to several square millimeters) acceptance window and, in principle, is therefore virtually insensitive to the size and coherence of the X-ray source. The Fraunhofer diffraction data are collected from a very large assembly of dispersed nanoparticles, and the recordable diffracted intensity is thus magnified by a factor approximately equivalent to the number of particles. If such data were recorded in a real-space imaging detector, it would produce a diffuse intensity distribution, similar to that achieved with SAXS, from which the mean size of the particles could be estimated. However, the X-ray phase cannot be retrieved, and the particle shape cannot be reconstructed.[15] The angular intensity distribution from a given particle does not depend on the beam size or the sample−detector distance, and the diffracted intensity measured in reciprocal space is thus simply the sum of the individual diffracted intensities from all particles exposed to the incident beam. In the case when all the particles are identical, the reconstructed image will represent an individual particle. However, when the dispersed particles have a spread in size, the reconstruction will show a "representative of the modal", that is the most frequently occurring particle.

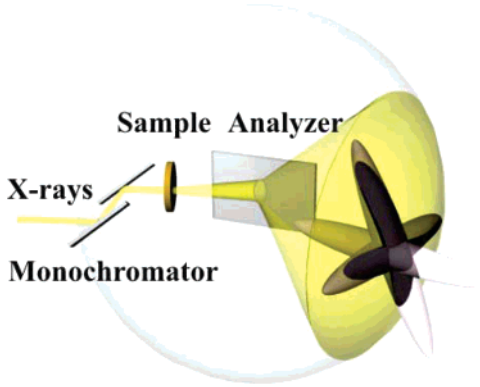

Figure 1. Schematic representation of the experimental configuration (not to scale). The crossed feature intersecting the Ewald sphere represents a 3-D diffraction image of a representative of the modal nanoparticle.

The mapping of reciprocal space with a crystal analyzer is widely employed experimentally for obtaining 2-D crystal structure information. It has been used, for example, to map the 2-D elastic strains in silicon (Si) crystals after ion implantation.[26] To obtain 3-D information about an object, it is necessary to exploit the full three dimensions of the Ewald sphere.[27] In contrast to conventional real-space imaging experiments,[6−17] the resulting 2-D map of the diffracted intensity from the sample represents a projection of the 3-D diffraction image on the Ewald sphere. Rotation of the sample about the principal optical axis sees a change in the 3-D intensity profile projected onto the surface of the Ewald sphere and, as a result, a change in the projected 2-D distribution of coherent diffracted intensity recorded from the sample. In the case of essentially 2-D structures, or nanoscale objects with spherical symmetry,[28] such 2-D projections of the 3-D intensity distributions are virtually indistinguishable. However, in the case of asymmetric nanoscale shapes, such as in the examples presented here, the projected intensity distribution recorded experimentally will change detectably with azimuthal rotation of the sample around the principal optical axis. This is again a contrast with real-space CDI, in which 2-D distributions of diffracted intensity are recorded using an imaging detector (e.g., a

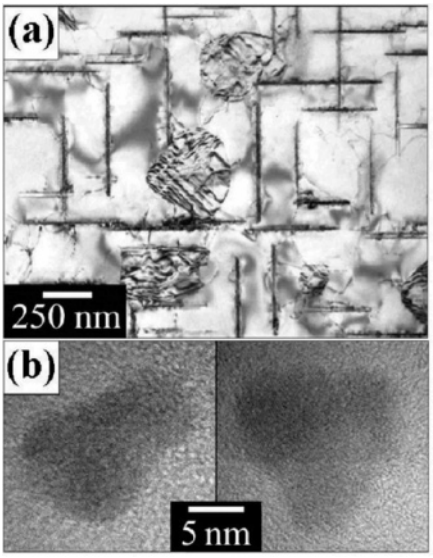

Figure 2. TEM micrographs of (a) an Al-4Cu sample aged 72 h at 250 °C and (b) TiO_2 nanoparticles embedded in a thin (100 nm) section of polymer matrix.

charge-coupled device or CCD), where such rotation of the sample only leads to rotation of an identical pattern of intensity, and a full tomographic reconstruction is required for 3-D analysis of the sample.[8]

To demonstrate the potential of this novel approach, we have selected a range of nanocomposite structures containing intermetallic and ceramic nanoparticles and carbon nanotubes, with characteristic dimensions ranging from on the order of 10 nm to a few hundreds of nanometers. Principal focus is on samples of a binary Al-1.7Cu (atom %) alloy,[29] solution treated, quenched and aged 72 h at 250 °C to form a rationally oriented distribution of Al_2Cu (θ') precipitates in dilute aluminum solid solution matrix, as shown in Figure 2a. The dispersed phase forms platelets of large aspect ratio parallel to {100} planes of the face-centered cubic matrix phase and the TEM image recorded parallel to a ⟨100⟩ matrix direction in Figure 2a reveals two orthogonal variants parallel to the electron beam and a third normal to the beam. From such images, recorded from 15 different regions, the θ' particle number density was estimated to be $\sim 1900 \pm 740$ particles/μm^3. On the basis of measurements from over 400 different θ' particles, the platelets were found to have an average diameter of $\sim 470 \pm 250$ nm and average thickness of $\sim 14 \pm 5$ nm. The errors reported correspond to the standard deviations for the data recorded and are relatively large because the particle size distribution in the samples examined was essentially bimodal. To complement examination of such samples, experiments were also conducted on separate polymer-based nanocomposite samples containing dispersions of titanium dioxide (TiO_2) nanoparticles, Figure 2b, and carbon nanotubes. Transmission electron microscopy of the TiO_2/polymer composite sample revealed a low number density of dispersed nanoparticles and the images of Figure 2b outline typical particles with dimensions in the range 5−15 nm that remain embedded within an ~100 nm thick section microtomed from the nanocomposite sample.

The experiments were performed using the experimental arrangement schematically presented in Figure 1. The Al−Cu experiment was performed on the undulator beamline BL29XU at SPring-8, Japan. Synchrotron radiation energy of 9 keV was selected using the primary double-crystal Si(111) beamline monochromator. Further angular collimation was performed by a double-crystal channel-cut Si 400 monochromator. Then the beam was spatially collimated by a pair of slits 100 μm wide (horizontal) and about 100 μm high (vertical-diffraction plane). The sample was placed just downbeam of the slits so that the incident beam was perpendicular to the sample plane shown in Figure 2. The Si (400) crystal analyzer and a PIN photodiode detector, with a 280 μm slit just before it, were placed downstream of the sample to collect the intensity diffracted from the sample as a 2-D function of the angular positions of the analyzer and detector−slit arrangement. The distance between the sample and the detector−slit arrangement was 400 mm. The angular range of the analyzer crystal of $\pm$ 0.5° and the detector−slit arrangement of $\pm$ 1.0° ($\theta - 2\theta$) with steps of 0.01 and 0.02°, respectively, were chosen to allow the reconstruction of the representative of the modal nanoparticle of expected size of 350 nm with a spatial resolution of 7.8 nm. The polymer nanocomposites containing dispersed TiO_2 and C nanoparticles were studied on the XDD beamline of the SSLS. A radiation energy of 8 keV was selected using the primary double-crystal Si(111) beamline monochromator. The 2-D intensity distributions were collected in reciprocal space around the Si(111) Bragg reflection of the crystal analyzer. The angular range of the analyzer crystal of $\pm$ 2.1° and the detector−slit arrangement of $\pm$ 4.2° with step of 0.03 and 0.06°, respectively, were chosen to allow the reconstruction of the representative of the modal nanoparticle/nanotube with a spatial resolution of 1 nm. In all such experiments the spatial resolution is determined by the conventional Fraunhofer diffraction relationship: $\Delta x = \lambda/\Delta\theta$, where λ is the radiation wavelength and $\Delta\theta$ is the total angular aperture of the experimental data.[28,30]

Figure 3 presents experimentally recorded 2D maps of the diffracted intensities for two azimuthal orientations of the Al−Cu alloy sample: defined as 0 degrees and 45°. The central vertical line in the maps is the main peak due to the Bragg reflection of the monochromator. To reconstruct the shape of the diffracting θ' nanoparticles embedded in the Al matrix, we used a modified Gerchberg−Saxton formalism.[5,28] In the present case, the diffracted intensity profiles can be approximated as the modulus squared of a Fourier transform of the complex transmission function. Since the modified G−S formalism can only reconstruct a real function,[8,28] we focused on the reconstruction of either the real or the imaginary part of the complex refractive index, $n = \delta + i\beta$. We assumed that for an Al_2Cu particle with a diameter of approximately 350 nm at 9 keV, the complex transmission function $\exp\{int(\vec{r})k\}$, where $t(\vec{r})$ describes the shape of the representative of the modal nanoparticle and k is the radiation wave-vector, can be expanded as $\exp\{int(\vec{r})k\} = 1 + i\delta t(\vec{r})k - \beta t(\vec{r})k$. The modal size of the nanoparticles was estimated from the width of the peaks in the 1D

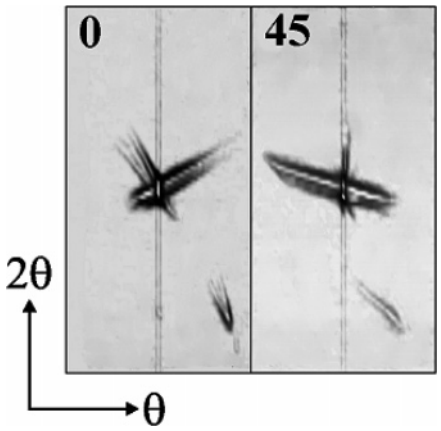

Figure 3. Projections of X-ray diffraction intensity (logarithmic scale) recorded experimentally from the dispersed Al_2Cu nanoparticles at two locations in reciprocal space separated by an azimuthal sample rotation of 45°. The "ghost" intensity detected in the lower right corner of the intensity profiles is attributable to higher order diffraction/refraction phenomena from the particle distribution.

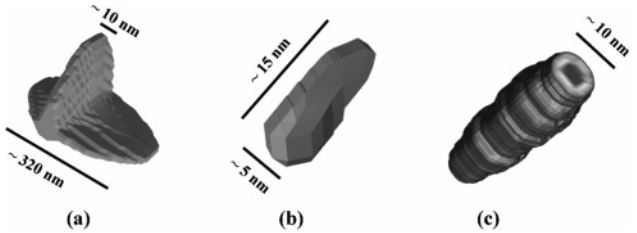

Figure 4. 3-D renderings of (a) two orthogonal variants of plate-shaped Al_2Cu nanoparticles embedded in an Al matrix. Surface faceting observable in the reconstructed image is of a form and scale consistent with growth defects associated with particle coarsening, but it remains to be established whether they can be interpreted to have such physical significance. (b) Representative of the modal TiO_2 nanoparticle dispersed in a polymer matrix. (c) Representative of the modal carbon nanotube dispersed in a polymer matrix.

diffraction scans performed prior to the 2-D data collection. Reconstruction of the TiO_2 nanoparticles and carbon nanotubes was performed using the same approach.

The result of the reconstruction for the Al−Cu sample is presented in Figure 4a. Reconstruction from the real or imaginary parts of the expanded complex transmission function gave indistinguishable results. The two orthogonal variants of the particle(s) reconstructed represent a representative of the modal particle in two orthogonal planes within the given aperture of the incident beam. The third θ' variant, equivalent to that normal to the plane of projection in Figure 2a, could not be reconstructed reliably from the data as it would require an additional rotation of the sample around an axis normal to the azimuthal axis and parallel to the habit plane of the variant. That the particles appear to be interpenetrating is an intrinsic feature of the reconstruction algorithm which manifests itself in both the analysis of the experimental data and the reconstructions performed from simulated data which are described below.

Reconstructions for the dispersed TiO_2 nanoparticles and carbon nanotubes are presented in Figure 4, parts b and c, respectively. The reconstructed form and dimensions of the representative of the modal TiO_2 nanoparticle are consistent with those of typical particles observed by TEM, Figure 2b. The difficulties experienced with conventional TEM imaging of embedded crystalline particles sparsely distributed in a polymer matrix serve to highlight qualitatively the sensitivity of the present technique to such dispersions of low number density and/or volume fraction. Equally, the example of Figure 4c illustrates qualitatively the capability of the technique for distinguishing crystalline carbon nanotubes dispersed in a largely amorphous molecular hydrocarbon. It should be realized, however, that the variations in the nanotube diameter correspond to single pixels in the reconstructed image, and thus cannot be claimed to be real features at present. The form and scale of the rendered image are consistent with those of the multiwall nanotubes typically used in composite nanostructures, where individual nanotubes vary from <10 nm to 10−20 nm in diameter, with aspect ratios (length: diameter) in the range 2:1 to 10:1. For both of these examples, the resolution in the reconstructed images was on the order of 1 nm.

Idealized simulations were conducted for the Al−Cu samples in an attempt to determine the correlation between the original and reconstructed particle sizes. The simulated diffraction pattern consisted of a normalized sum of 200 individual diffraction patterns, each of which was obtained by taking the Fourier transform of a 2-D transmission function. The model transmission functions were randomized distributions of 10−20 orthogonal variants of the θ' nanoparticles, whose range of sizes was described by a Gaussian distribution: $1/\sigma\sqrt{2\pi}\ \exp(-((x-\mu)^2)/2\sigma^2)$, with mean nanoparticle diameters of 300 or 400 nm, and standard deviation, σ, varying from 1 to 180 for each mean diameter. The simulation reconstruction results showed that for both mean diameters, S_m, the representative of the modal reconstructed nanoparticle size, S_r, was related to the size deviation via $S_r/S_m \approx 1 + 0.001\sigma^{1.33}$ (Figure 5).

The technique described here represents an important addition to the emerging suite of tools available for 3-D X-ray characterization of nanostructures. The principal advantage of the method is that it allows for nondestructive and in situ analysis over large (several cubic millimeters) volumes of material, and determination of the representative of the modal size and shape of a dispersed array of nanoscale (<100 nm) scattering objects with potentially sub-10 nm spatial resolution. Moreover, it is, in principle, insensitive to the coherency of the radiation employed and can thus be implemented in a laboratory environment. While it does not permit direct imaging of individual objects in an array, the technique does have potential for rapidly determining in situ temporal changes in the modal dimensions and form of a scattering array as a function of changes in such external variables as temperature, pressure and applied stress. That it is able to do so in volumes of material truly representative of bulk behavior ensures that the technique is highly complementary to alternative approaches which are commonly destructive of the material in specimen preparation and often restricted to highly localized and potentially unrepresentative volumes. A typical area of the material

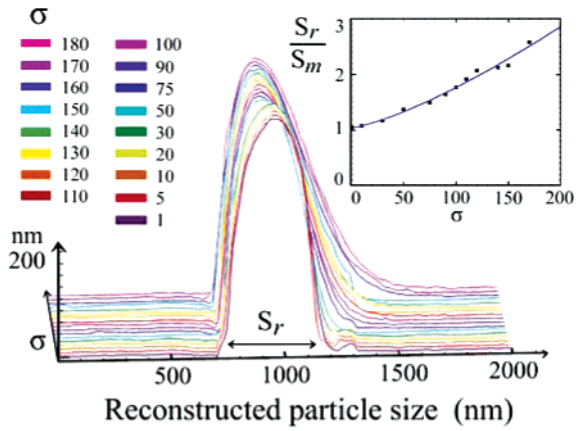

Figure 5. Correlation between the reconstructed representative of the modal nanoparticle diameters, and the statistical spread, σ, of nanoparticle diameters in the idealized simulated samples. For ease of comparison, 1-D nanoparticle profiles are shown, extracted from 2-D reconstructions for various diameter distributions (Gaussian spread of diameters, with standard deviation 1 to 180). Here, an ideal projected nanoparticle diameter profile is $2\sqrt{S_m^2-(x-x_0)^2}$ where S_m is the mean diameter (400 nm), x is pixel position, x_0 is the center of the simulated sample area (2 μm × 2 μm).

studied in a TEM experiment covers tens to hundreds of nanometers. A single experiment employing the present technique eclipses this total volume by at least 1 order of magnitude, up to a few cubic millimeters, providing the ideal input for modern computational materials science, which seeks to model material behavior in terms of structure averaged over representative volumes.

Acknowledgment. The authors acknowledge the support of the Australian Research Council (ARC), the Australian Synchrotron Radiation Program, Nanotechnology Victoria Ltd., and the Department of Innovation (Victoria). N.A.Z. is the recipient of an Australian Postgraduate Award, and B.C.M. is the recipient of an ARC Federation Fellowship. The work was also supported by RIKEN and the SPring-8 synchrotron facility. We thank Y. Ping for the help during the SSLS experiment.

References

(1) Embury, J. D.; C. W. Sinclair, C. W. *Mater. Sci. Eng.* **2001**, *A319−21*, 37−45.
(2) Williams, D. B.; Carter, C. B. *Transmission Electron Microscopy, Part I−Basics*; Plenum Press: New York and London, 1996; pp 1−173.
(3) Miller, M. K. *Atom Probe Tomography−Analysis at the Atomic Level*; Kluwer Academic/Plenum: Dordrecht, The Netherlands, 2000.
(4) Renaud, G.; Lazzari, R.; Revenant, C.; Barbier, A.; Noblet, M.; Ulrich, O.; Leroy, F.; Jupille, J.; Borensztein, Y.; Henry, C. R.; Deville, J.; Scheurer, F.; Mane-Mane, J.; Fruchart, O. *Science* **2003**, *300*, 1416−1419.
(5) Fienup, J. R. *Appl. Opt.* **1982**, *21*, 2758−2769.
(6) Miao, J.; Charalambous, P.; Sayre, D. *Nature (London)* **1999**, *400*, 342−344.
(7) Robinson, I. K.; Vartanyants, I. A.; Williams, G. J.; Pfeifer, M. A.; Pitney, J. A. *Phys. Rev. Lett.* **2001**, *87*, 195505(4).
(8) Miao, J.; Ishikawa, T.; Johnson, B.; Anderson, E. H.; Lai, B.; Hodgson, K. *Phys. Rev. Lett.* **2002**, *89*, 088303(4).
(9) Williams, G. J.; Pfeifer, M. A.; Vartanyants, I. A.; Robinson, I. K. *Phys. Rev. Lett.* **2003**, *90*, 175501(4).
(10) He, H.; Marchesini, S.; Howells, M. R.; Weierstall, U.; Chapman, H. N.; Hau-Riege, S. P.; Noy, A.; Spence, J. C. H. *Phys. Rev. B* **2003**, *67*, 174114(3).
(11) Marchesini, S.; He, H.; Chapman, H. N.; Hau-Riege, S. P.; Noy, A.; Howells, M. R.; Weierstall, U.; Spence, J. C. H. *Phys. Rev. B* **2003**, *68*, 140101(4).
(12) Nugent, K. A.; Peele, A. G.; Chapman, H. N.; Mancuso, A. P. *Phys. Rev. Lett.* **2003**, *91*, 203902(4).
(13) Eisebitt, S.; Lörgen, M.; Eberhardt, W.; Lüning, J.; Andrews, S.; Stöhr, J. *Nature (London)* **2004**, *432*, 885−888.
(14) McBride, W.; O'Leary, N. L.; Allen, L. J. *Phys. Rev. Lett.* **2004**, *93*, 233902(4).
(15) van der Veen, F.; Pfeiffer, F. *J. Phys.: Condens. Matter*. **2004**, *16*, 5003−5030.
(16) Miao, J.; Nishino, Y.; Kohmura, Y.; Johnson, B.; Song, C.; Risbud, S. H.; Ishikawa, T. *Phys. Rev. Lett.* **2005**, *95*, 085503(4).
(17) Pfeifer, M. A.; Williams, G. J.; Vartanyants, I. A.; Harder, R.; Robinson, I. K. *Nature (London)* **2006**, *442*, 63−66.
(18) Jacobsen, C.; Kirz, J. *Nature Struct. Biol.* **1998**, *5*, 650−653.
(19) Larson, B. C.; Yang, W.; Ice, G. E.; Budai, J. D.; Tischler, J. Z. *Nature* **2002**, *415*, 887−890.
(20) Chao, W.; Harteneck, B. D.; Liddle, J. A.; Andersen, E. H.; Attwood, D. T. *Nature (London)* **2005**, *435*, 1210−1213.
(21) Schroer, C. G.; Kurapova, O.; Patommel, J.; Boye, P.; Feldkamp, J.; Lengeler, B.; Burghammer, M.; Riekel, C.; Vincze, L.; van der Hart, A.; Kühler, M. *Appl. Phys. Lett.* **2005**, *87*, 124103(3).
(22) Maser, J.; et al. *Proc. 8th Int. Conf. X-ray Microscopy, IPAP Conf. Ser. 7*; **2005**, 26−29.
(23) Zuo, J. M.; Vartanyants, I. A.; Gao, M.; Zhang, R.; Nagahara, L. A. *Science* **2003**, *300*, 1419−1421.
(24) Faulkner, H. M.; Rodenburg, J. M. *Phys. Rev. Lett.* **2004**, *93*, 023903(4).
(25) Wu, J. S.; Weierstall, U.; Spence, J. C. H. *Nat. Mater.* **2005**, *4*, 912−916.
(26) Nikulin, A. Y.; Sakata, O.; Hashizume, H.; Petrashen, P. V. *J. Appl. Cryst.* **1994**, *27*, 338−344.
(27) Nikulin, A. Y.; Davis, J. R.; Cookson, D. J. *Phys. Stat. Sol. a* **1998**, *169*, 3−8.
(28) Dilanian, R. A.; Nikulin, A. Y. *Appl. Phys. Lett.* **2005**, *87*, 161904(3).
(29) Gayle, F. W.; Goodway, M. *Science* **1994**, *266*, 1015−1017.
(30) Nikulin, A. Y.; Darahanau, A. V.; Horney, R. B.; Ishikawa, T. *Physica B* **2004**, *349*, 281−295.

NL070131Z